RSC Advances

ROYAL SOCIETY OF CHEMISTRY

www.rsc.org/advances

RSC Advances

RSCPublishing

ARTICLE

Structure determination of molecular nanocomposites by combining pair distribution function analysis and solid-state NMR

Cite this: DOI: 10.1039/x0xx00000x

Received 00th January 2012,
Accepted 00th January 2012

DOI: 10.1039/x0xx00000x

www.rsc.org/

E-.E. Bendeif,[a,b] A. Gansmuller,[a,b] K.-Y. Hsieh,[a,b] S. Pillet,[a,b] Th. Woike[c] M. Zobel,[d] R. B. Neder,[d] M. Bouazaoui,[e] H. El-Hamzaoui,[e] and D. Schaniel,[a,b]

Transparent mesoporous silica monoliths of well controlled porosity and a narrow pore size distribution around 6 nm have been used to prepare sodium nitroprusside (SNP) nanocomposites. The obtained nanomaterials could be characterised using X-ray total scattering coupled to atomic pair distribution function analysis (PDF) and solid-state NMR spectroscopy. The PDF analysis allows for a structural description of the confined species as well as for the identification of various existing phases: SNP isolated molecules and SNP crystalline nanoparticles. The model obtained suggests that the nanocrystals have the same molecular structure as the bulk crystalline material and measure about 6 nm in diameter. This result is quite exceptional since the space available inside the pores is only about ten times the size of the molecules. The multi-nuclei Solid State NMR investigation confirms the structural model proposed by the PDF analysis and assigns the isolated molecules to dynamic disorder of a solvated phase. The latter approach additionally provides quantitative information on the relative ratio between the dynamic molecules and the rigid nanocrystals. This result is exploited to study the evolution of the two confined SNP phases with respect to solvating water molecules. We show that the confined SNP nanocrystals can be easily dissolved when storing the nanocomposites at increasing atmospheric relative humidity.

1. Introduction

Porous silica gels have excellent biocompatibility, they are easy to prepare, transparent over a wide spectral range, and the pore size (1 -100 nm) can be adjusted for targeted incorporation of nanoparticles or molecules[1,2]. Moreover, silica gels can be themselves prepared as nanoparticles with pore sizes in the nanometer range and appropriate surface coatings for targeting and entering different type of cells[3] as well as sensitive to a variety of triggers (photochemical, photothermal, enzymatic, …)[4]. These properties make porous silica composites ideal host materials for Active Pharmaceutical Ingredients (API), such as nitrix oxide (NO) donors[5].

In order to be useful as API-carrying material one must assure that the pharmaceutical activity – or on more general grounds the desired property – of the functional guest molecule is maintained after encapsulation in the porous host network. Important parameters that may influence the activity are the size of the nanoparticle and its solubility as well as the surrounding pH-value and relative humidity. The release kinetics and therefore the bioavailability of an API will, for example, strongly depend on the ability of the nanoparticles to dissolve in the pores and the solvated molecules to leave the porous host network. Furthermore, the host material might affect the structural integrity of the active ingredient or adsorb it on its inner surface, inhibiting the desired application. As has been shown for "simple"[6] (e.g. benzene) and more complex[7] (e. g. isobutyric acid) liquids, phase transition temperatures can be modified when the liquid is entrapped inside a porous matrix. This so called "confinement effect" has also been observed for encapsulated organic solids, including anti inflammatory API[8–10], where the particle structure and even the physical state of the molecules were different than in the bulk material. The confinement effect on melting and glass transition temperatures mainly depends on the pore size and the relative strength between the guest/guest and host/guest interactions[11,12]. For weak host/guest interactions these temperatures are typically lower than for the bulk material. When the pore size is reduced, the decrease of the melting temperature becomes even greater, in qualitative agreement with the Gibbs–Thomson equation[13,14]. According to a study combining Dielectric Relaxation Spectroscopy and Differential Scanning Calorimetry experiments with Grand Canonical Monte Carlo simulations[15], fluids confined in cylindrical nanopores (e.g. MCM41) should freeze into a single crystalline structure for average pore diameters larger than 20σ (σ being the diameter of the guest molecule). However, fluids or mixtures[16,17] in pores with a diameter between 15σ and 20σ should essentially crystallize

into a frustrated crystal structure with the rest forming an amorphous or liquid region. Finally, for pore sizes smaller than 15σ, even partial crystallization should not occur. These boundaries can however be modulated by the composition and the roughness of the pore surface.

It is thus desirable to dispose of experimental methods allowing for a detailed structural characterisation of the functional guest and its interaction with the host, especially as a function of external parameters like temperature and environmental humidity. We have recently shown that the structure of inorganic complexes, isolated inside 1nm pores, can be analysed by total scattering methods and subsequent modelling with the pair distribution function (PDF). We additionally demonstrated that, in combination with nuclear magnetic resonance (NMR), the structure, the dynamics, and the interaction of isolated solvated molecules with its porous hosts could be characterized[18]. We show here for $Na_2[Fe(CN)_5NO]\cdot 2H_2O$, sodium nitroprusside (SNP), that crystalline nanoparticles can be grown inside an amorphous silica matrix with a pore diameter as small as 6nm. We also demonstrate that the structure inside the matrix is heterogeneous and that the ratio between nanoparticles and solvated molecules can be determined by combining PDF-analysis and NMR spectroscopy as a function of atmospheric relative humidity.

SNP is an API used for regulation of blood pressure[19] and is discussed for a variety of other medical applications due to its possibility to release the NO-ligand[20]. Furthermore, SNP has photochromic and photorefractive properties rendering the material interesting for optical applications such as data storage or all-optical switching[21,22]. We have already studied SNP incorporated into silica matrices with pore sizes of 1 nm by combining PDF and NMR[18]. The detailed structural analysis using x-ray total scattering and PDF-analysis clearly showed that SNP occurs as isolated solvated complexes keeping its structural integrity and only changing the cation-anion arrangement with respect to the crystalline phase. Thereby the Na^+ cations arrange themselves in the equatorial plane of the $[Fe(CN)_5NO]^{2-}$ anion, cis to the NO. Since the SNP complexes in this case were isolated from each other, the PDF spectrum exhibits mainly intramolecular distances and serves thus as an unambiguous fingerprint of the encapsulated molecular complex. These results were further confirmed by a multinuclear NMR study. NMR is especially suited due to its local character and its sensitivity towards the ^{23}Na, ^{13}C, ^{1}H, and ^{29}Si isotopes present in the studied material. From the ^{29}Si spectra we could infer that the host matrix was not changed by the incorporation of the guest and the ^{23}Na spectra confirmed the absence of crystalline SNP phase. The ^{1}H spectra on the other hand showed that there is always a certain amount of water molecules present inside the porous network, which can hardly be completely removed. Finally the ^{13}C spectra showed evidence for isotropic rotational diffusion of the solvated SNP complexes inside the matrix pores. Therefore, the H_2O present in the pores could not be reasonably modelled by the PDF analysis.

If the size of the pores in the network is increased, e.g., in order to enhance drug releasing capabilities or drug concentration, the SNP complexes can aggregate or even crystallise in the form of nanoparticles. In this case important questions are how much of the active ingredient occurs in crystalline form, and how can this amount be controlled. Consequently, in order to study these questions and to extend our characterisation approach, we prepared silica xerogels with pore sizes of 6 nm and loaded them with SNP (from aqueous solution). We are demonstrating in the following, using PDF and NMR, that crystalline SNP nanoparticles can be grown inside pores of 6 nm. We observe that both solvated molecules and nanoparticles of about 6 nm diameter are incorporated and grown inside the matrix. NMR detects again the presence of water, which amount depends on the environmental humidity. From the ^{23}Na and ^{13}C spectral signatures, an unambiguous assignment of the liquid and solid SNP phases can be made, and the corresponding ratio can be determined.

2. Experimental

2.1. Synthesis of mesoporous silica monoliths:

The monolithic porous silica matrices host were synthesized according to the procedure previously reported[23–25]. The transparent mesoporous monoliths were obtained by hydrolysis and polycondensation of TMOS, followed by a drying step and annealing in air at 850°. This sol–gel process yields a large range of mesoporous xerogels with well controlled pore sizes.

2.2. Preparation of SNP-silica nanocomposites

The SNP@SiO2 nanocomposites were obtained following the wet impregnation procedure we already published[18]. The prepared empty monoliths were loaded in an aqueous solution of SNP salt (c = 3.507 $mol.L^{-1}$). The silica matrices were slowly added into the SNP solution in order to prevent any cracking. The monoliths, initially transparent, then became progressively more and more brown-orange indicating the diffusion of the SNP complexes into the silica pore network. After about 24 hours the monoliths displayed homogeneous colouring and were kept at 50 °C for 7 days in an oven. A final drying step was performed at room temperature in desiccators coupled with a primary pump (ca. 10^{-2} mbar) for about 3 days in order to remove the remaining solvent. A cross section of the doped monolith exhibits a uniform brown-orange color, confirming a homogeneous distribution of SNP complexes. **Fig 1** shows the empty and the doped monoliths.

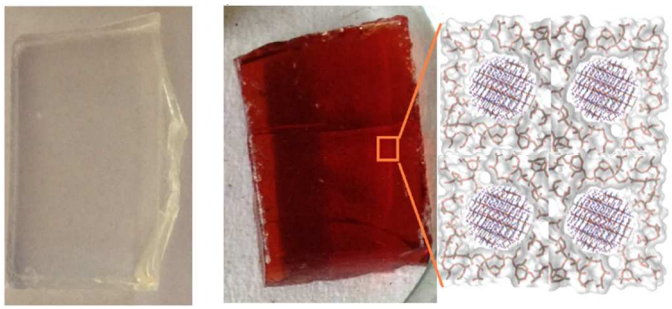

Fig 1. Photographs of transparent empty silica monolith (left) and SNP-silica nanocomposite (right).

2.3. Nitrogen adsorption-desorption analysis

In order to characterize the porosity of the undoped xerogels, nitrogen sorption isotherms (Figure 1S (a)) were recorded at 77 K using a Quantachrome porosimeter Autosorb 1-LP-MP, after an outgassing process of several hours at 150°C under secondary vacuum. Specific surface area was determined by the Brunauer–Emmett–Teller (BET) method[26]. The total pore volume was determined at P/P_0 = 0.99938. The pore size diameter and distribution were calculated according to the Barrett–Joyner–Halenda (BJH)[27] model. As previously reported for this type of xerogel[25], the specific surface area and the total pore volume are estimated to 360 m^2g^{-1} and 0.49 cm^3g^{-1} respectively[26] by the BET method[26]. The pore size distribution, derived by the BJH method[28], is centered around 5.8 nm with a narrow size distribution (Figure 1S (b)). More details on the nitrogen adsorption-desorption analysis are given in the supplementary materials (S.I).

2.4. Total scattering X-ray measurements and PDF analysis

The total scattering X-ray measurements were performed at the High Energy Scattering Beamline ID15B of the European Synchrotron Radiation Facility (ESRF). The data sets were collected using a Perkin Elmer flat panel detector and a high energy monochromatic beam (56 keV, λ = 0.22299 Å). Such experimental setup allows to record total scattering patterns for the unloaded and loaded monoliths to high momentum transfer (Q~24 $Å^{-1}$), which is crucial for providing high and adequate real-space resolution of the PDF peaks for a quantitative structural analysis. The collected data were then corrected for experimental effects and the differential experimental atomic pair distribution function (d-PDF) was obtained following the procedure we reported earlier[18]. All data processing was done using Fit-2D[28] and GudrunX[29] softwares.

2.5. Solid state NMR spectroscopy

All experiments were carried out on a high-field Bruker NMR Avance III spectrometer operating at 14 T (^{1}H NMR frequency of 600MHz) with a Bruker 4mm MAS triple-resonance probe. MAS spinning speed was set to 12.5 kHz.

For ^{13}C MAS experiments the rf-field strength applied for the ^{13}C pulse was set to 46 kHz, leading to a 90° pulse length of 5.4 µs. During acquisition, SPINAL-64[30] heteronuclear decoupling was applied at an rf-field strength of 80 kHz. For the hybrid SNP@SiO_2 sample the interscan delay (rd) was set to 5 s and 84 s and 1600 scans were accumulated for a total experimental time of about 2h and 37 h respectively.

For ^{23}Na MAS experiments the rf-field strength applied for the ^{23}Na pulse was set to 50 kHz with an excitation pulse length of 1 µs (18° flip angle). During acquisition, SPINAL-64[30] heteronuclear decoupling was applied at an rf-field strength of 80kHz. The interscan delay was set to 5s; 128 scans were accumulated for a total experimental time of about 10min.

For the hydration study **(Fig. 8)** the open NMR rotors were stored overnight with saturated solutions of LiBr, $CaCl_2$ and KCl salts stabilizing the atmosphere at 6%, 29% and 85% relative humidity (25°C) respectively. For all experiments, the temperature at the stator output was stabilized at 298K.

The Dmfit[31] program was used for spectral deconvolution as well as fitting of ^{13}C chemical shift anisotropy and second order quadrupolar effects on the lineshapes of the ^{23}Na central peaks. All spectra were processed with the GSim program developed by V. Zorin[32].

3. Results and discussion

3.1. Experimental differential PDF (d-PDF)

The total scattering patterns of the empty and the loaded monoliths are given if **Fig 2a**. Both patterns exhibit the typical amorphous silica features as also observed for the SNP complexes incorporated

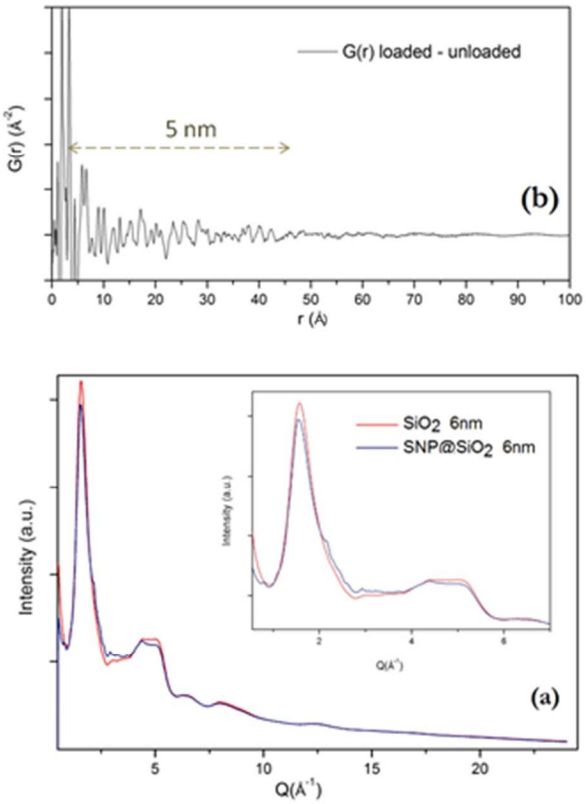

in silica monoliths with pore sizes in the range of 1~3 nm[18] . Besides the main peak at Q~1.64 Å^{-1} one can also observe additional broad peaks in the Q-range 2.5-4 Å^{-1} in the loaded monolith indicating the formation of a nanocrystalline SNP phase inside the silica monolith. The resulting differential atomic d-PDF is shown in **Fig. 2b**. For the subsequent analysis and discussion of the results we divide this experimental d-PDF into three regions: the short range (interatomic distances below ~8 Å), the medium range (8-50 Å) and the long range (> 50 Å) region. The short range region gives information on the first few coordination spheres and contains thus mainly the information about the intramolecular SNP structure and the first neighbours in the crystal such as cations. The medium and long ranges contain information on the periodicity of the synthesised particles and on their size. From the d-PDF diagram we can clearly observe well defined features up to about 50 Å, which reflects the crystalline character of the SNP within the SNP-silica nanocomposites. The rapid falloff of d-PDF oscillations beyond r ~ 50 Å indicates that the range of the structural coherence is limited to ~ 5 nm. Indeed, a finite crystallite size diminishes the number of atom pairs separated by distances larger than the crystallite diameter and, consequently, leads to abruptly damping PDF features. We therefore refer, as a first approximation, to the confined SNP particles as 5 nm in diameter. In order to obtain the structural model corresponding to the differential PDF we performed the following modelling strategy by using the *DISCUS* program[33]. At first, the d-PDF pattern was fitted by simulating a spherical SNP crystal with a diameter of 5nm. This model was constructed on the basis of the molecular structure of the bulk crystalline material at room temperature (297 K).

Fig 2. (a) The total scattering patterns of unloaded (red) and loaded (blue) monoliths. **(b)** The corresponding differential-PDF.

The spherical shape was obtained by applying a spherical envelope function of 5 nm diameter, in other words a spherical nanoparticle was cut out of the infinite perfect crystal. One have to note that the

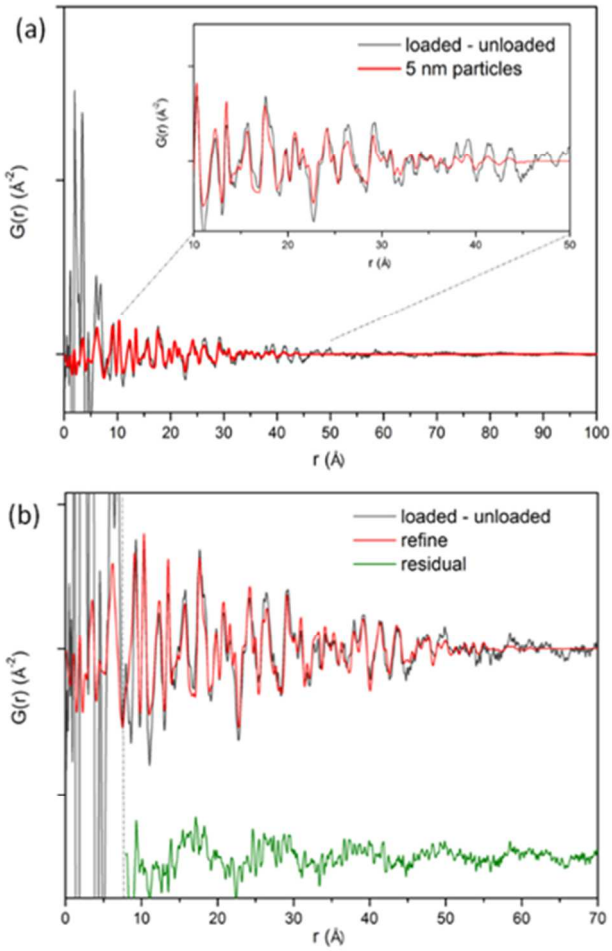

spherical envelope function gives the best fit of the calculated PDF to the experimental data, compared to anisotropic envelope functions like, e.g., cylinders, that we have tested. The resulting simulated d-PDF pattern is shown in **Fig. 3a** in comparison to the experimental d-PDF. We observe that this model does not describe well the short range region, especially the amplitudes are largely underestimated. These residual sharp peaks at low r value might be due to the presence of a second contribution (phase) confined in the porous environment. This will be discussed in details in the next paragraph. The medium range region on the other hand is rather well described, although the oscillations damp off too fast with respect to the experiment (**see the inset in Fig. 3a)**. Since the damping is directly related to the particle size we refined the nanoparticle size (i.e. the diameter of the envelope function) using the experimental data in the range of 8-70 Å, thereby excluding the short range region which would bias the result. This refinement provided an improved fit and

an average particle size of about 6 nm (**Fig. 3b)**. This result is in good agreement with the pore size distribution obtained from nitrogen sorption measurements (**see S.I**).

Having now a good description for the medium and long range regions, we come back to the residual sharp peaks observed in the short range region (r < 8 Å). In order to determine the structural model corresponding to these residual peaks we subtracted the modelled PDF contribution of the 6 nm crystalline particles from the experimental d-PDFs pattern as shown in **Fig. 4**. The resulting difference exhibits a close resemblance with the PDF modelled with isolated SNP molecules[18], indicating that the additional contribution is due to the presence of isolated SNP molecules distributed in the porous network (**see the inset in Fig. 4)**.

Fig 3. (a) The experimental d-PDF (black) fitted with a 5nm spherical particle model based on the bulk crystalline structure (red) **(b)** A similar fit with refinement of the nanoparticle size using the experimental data in the range of 8-70 Å.

3.2. Solid State NMR approach

Following the strategy we established in our last study of SNP inside a 1 nm pore size matrix[18], we perform a complementary multinuclear MAS-NMR study. The purpose is (i) to confirm the structural features obtained from the PDF analysis, and (ii) to characterize the physical state of the confined SNP complexes depending on hydration levels.

As a first step we validate the differential PDF approach by comparing the ^{29}Si spectra of the empty and the loaded matrices (spectra not shown). Indeed, as in our last study, we verify that the spectrum of the loaded matrix does not show any additional chemical sites nor an increase of the line widths. This indicates that no modification of the matrix is induced by the SNP embedding procedure.

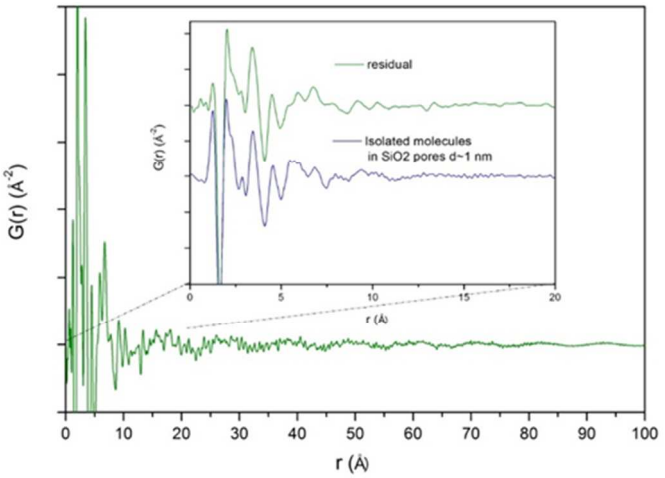

Fig 4. The d-PDF pattern obtained after the subtraction of the 6 nm nanocrystalline particles contribution from the experimental d-PDF. The inset shows the comparison between the resulting d-PDF (in green) and the PDF of isolated SNP molecules from ref 18.

The second step corresponds to the characterization of the SNP guest complex. For this purpose two NMR active nuclei are chosen: ^{13}C NMR focuses on the $[Fe(CN)_5NO]^{2-}$ anions and ^{23}Na NMR probes the Na counterions.

The ^{13}C MAS-NMR spectra present very different features depending on the acquisition parameters, especially when the interscan recycling delay is varied **(Fig 5)**. For shorter recycling interscan delays (e.g. 5s), the detected isotropic ^{13}C signal is centred on the chemical shifts in the solution state (~134ppm). No MAS sidebands reflecting the large Fe-^{13}C≡N chemical shift anisotropy (δ^{csa} = 208 ppm) are observed. This recalls the results obtained for the SNP confined in the 1nm pore size matrix; it shows evidence for sub-µs isotropic rotational diffusion and indicates the presence of a "liquid like" state through solvation by free water molecules[18]. When longer recycling delays are used (e.g. 84s), the detected isotropic ^{13}C signal shifts towards the bulk crystalline values (~136ppm) and MAS sidebands appear. These sidebands, marked by asterisks on figure 5, reflect the strong Fe-^{13}C≡N chemical shift anisotropy and can only appear if the phase is rigid with an accordingly longer T_1 relaxation time. Therefore theses spectral differences for short and long relaxation delays respectively reveal the coexistence of a mobile and a rigid phase of SNP.
Despite the fact that these results clearly confirm the presence of two different SNP phases, the poor ^{13}C sensitivity prevents precise quantification of the amount ratio between the phases. The large linebroadening consequently applied for the processing (~300Hz) also limits the spectral resolution of the central line. It is therefore not possible, from the ^{13}C spectra alone, to characterize the degree of order in the rigid phase and to distinguish between an amorphous and a crystalline structure of the rigid phase. Nevertheless, since the longitudinal relaxation times of the phases differ by about two order of magnitudes (T_1=300ms/37s for the mobile/rigid phases respectively), a bi-exponential fitting of a saturation recovery experiment can provide an estimation of the relative ratio of the two phases. This analysis shows that less than 35% of SNP molecules are in a mobile phase.

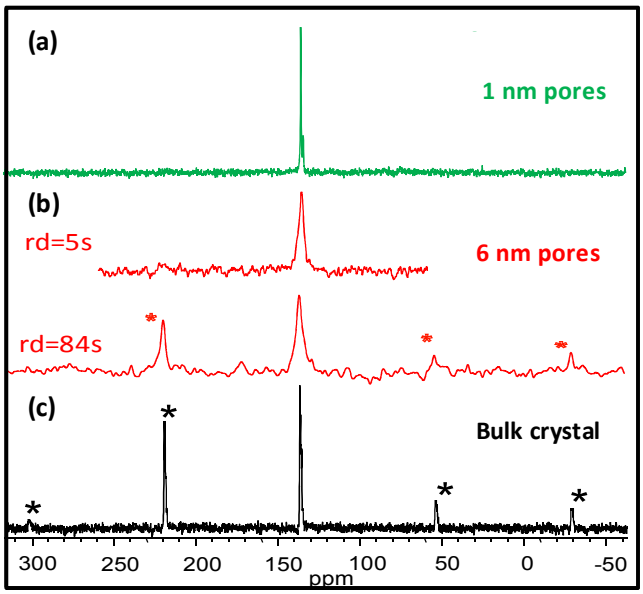

Fig 5. ^{13}C MAS NMR spectra (ν^{MAS} = 12.5 KHz) of the SNP recorded in different environments: (a) loaded into a 1nm pore SiO_2 matrix from ref 18, (b) loaded into a 6nm pore SiO_2 matrix and (c) inside the bulk crystalline material. For (b) the spectra have been recorded with recycling interscan delays of 5s (top) and 84s (bottom) respectively. Spinning sidebands are marked by asterisks.

The ^{23}Na MAS-NMR spectra also present evidence for the coexistence of a rigid and a "liquid like" phase, but the good sensitivity of the nuclei permits the structural characterization of the rigid phase **(Fig 6)**. The rigid phase component of the spectrum shows two distinct sites, Na_1 (δ_1^{iso} = -5.7 ppm) and Na_2 (δ_2^{iso} = -1.9 ppm). The first site has a quadrupolar constant C_{Q1} = 1369 kHz and an asymmetry of η_1 = 0.9 illustrated by the characteristic central lineshape, while the second site Na_2 has a smaller constant C_{Q2} = 615 kHz and η_2 = 0.3 and exhibits visible quadrupolar satellites.

The chemical shifts and quadrupolar constants are the same as for the ^{23}Na nuclei inside the bulk crystalline SNP structure; therefore we can conclude that the rigid SNP phase in the nanocomposite is crystalline with an identical structure as in the bulk crystal. Given the high sensitivity of the ^{23}Na nuclei, it is relatively easy to deconvolute the central resonance lines in order to extract the relative ratio between the crystalline and mobile phases **(Fig 7)**. Taking into account the ^{23}Na magnetisation distributed in the satellite transitions, we find that, for the sample studied, 25% of the SNP complexes are in a "liquid like" state.

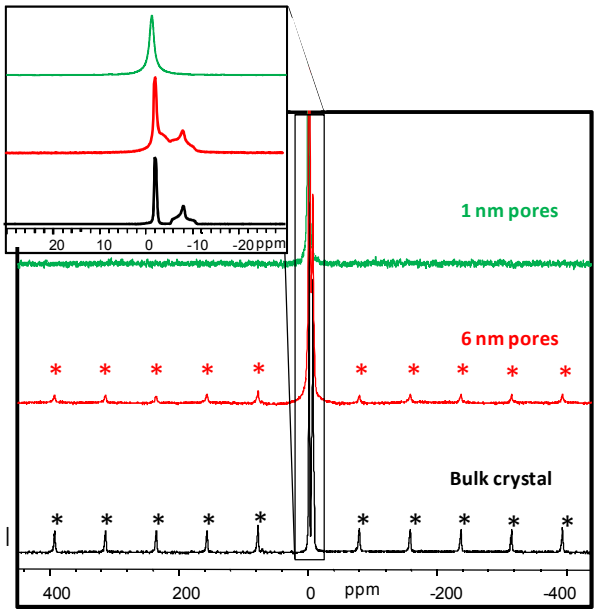

Fig 6. ^{23}Na MAS NMR spectra (ν^{MAS} = 12.5 KHz) of the SNP recorded in different environments: (a) loaded into a 1nm pore SiO_2 matrix from ref 18, (b) loaded into a 6nm pore SiO_2 matrix and (c) inside the bulk crystalline material. MAS satellite sidebands are marked by asterisks. The inset focuses on the centre band of the spectra.

Since we know from our previous study that water molecules can easily exchange between the matrix pores and the atmosphere, we also decided to study the effect of hydration on the confined nanoparticles. **Figure 8** presents ^{23}Na MAS-NMR spectra for samples stored in three different environments of 6%, 29% and 84% relative humidity (RH). The spectral deconvolution permits monitoring of the effect of hydration on the distinct phases of the confined SNP. The increase of relative humidity affects the solvated phase in a similar way to what we observed for 1nm pore nanocomposites[18] because the signal becomes narrower and shifts towards the aqueous solution reference at 0 ppm (NaCl 1M). The frequency range indicates the maintenance of a six fold coordination of the Na^+ cations, but the displacement to higher frequencies of this component (in green) reflects a reduction of the average Na-O distances[34,35]. Additionally, since the simultaneous line narrowing indicates increased dynamics of the cations, we can therefore conclude that the increase in relative humidity leads to a better solvation of the cations in the mobile phase until they are completely surrounded by water molecules. On the contrary, the signals from the crystalline phase are not modified by hydration, which indicates no change in the nanoparticle structure. However, it is very interesting to notice that the ratio between crystalline and solvated complexes is modified by

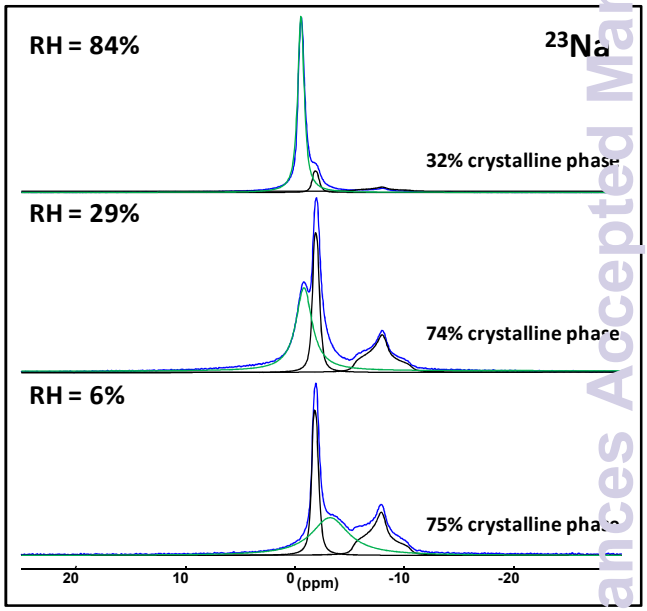

atmospheric humidity. For relatively dry atmosphere up to 29% relative humidity the relative surfaces of the peaks don't change since the narrowing of the mobile component is compensated by an increased intensity. Therefore the amount of molecules in a crystalline state does not vary and stays around 75%, which suggests that the last 25% of SNP complexes are located in a space of the gel matrix that prevents particle crystallization.

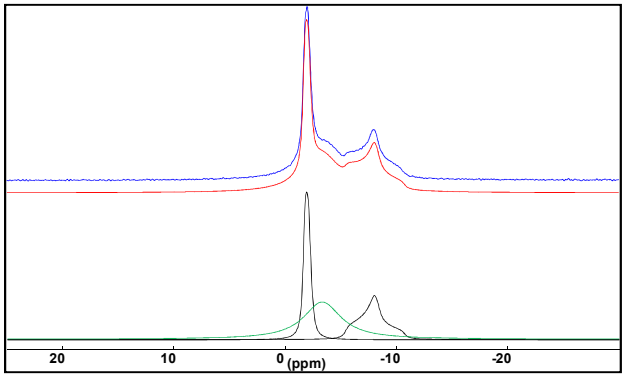

Fig 7. ^{23}Na MAS NMR spectra (ν^{MAS} = 12.5 KHz) of the SNP loaded into a 6nm pore size SiO_2 matrix. The top spectrum corresponds to the experiment and the middle spectrum to a model based on the sum of the fitted components. The bottom spectra show an overlap of the fitted components.

This space could be located at the interface between the nanoparticles and the pore surface or in residual pores of smaller size. When humidity is raised up to 84% RH, the amount of Na atoms in a crystalline state drops down to 32%. This variation between intermediate and high hydration points towards the formation of a liquid like contact layer of SNP around the pore surface. It also implies that atmospheric humidity can very easily dissolve the nanocrystals inside the pores, a behaviour that is not observed for the bulk macrocrystals.

Fig 8. Effect of hydration on ^{23}Na MAS NMR spectra (ν^{MAS} = 12.5 KHz) of the SNP loaded into a 6nm pore size SiO_2 matrix. The experimental spectra are overlaid with the fitted decomposition. The loaded xerogels have been stored overnight at 84%, 29% and 6% relative humidity (Top to bottom)

3.3. Discussion

The combination of total X-ray scattering coupled to PDF analysis and solid-state NMR spectroscopy allows for the characterisation of nanoscale hybrid materials. In the following we discuss the requirements and precautions to be applied to such a study as well as some caveats in the interpretation of the results.

The structural analysis is based on the experimental differential PDF obtained by direct subtraction of a reference PDF measured for the empty silica matrix from that of the guest-loaded framework, eliminating therefore the contributions arising from host-host atomic correlations (interatomic distances), and hence, recovers the structural properties of the guest. This requires that the matrix itself is not significantly affected by the impregnation with the guest. This is verified by ^{29}Si-NMR analysis. The differential PDF then contains the structural information (distances between pairs of atoms) of the guest but also of possible pairs between host and guest, e.g. Fe-Si distances, as these are not cancelled out by the subtraction procedure. In the presented study these distances did not appear distinctly in the G(r) because we are dealing with an amorphous matrix and a randomly oriented guest. This configuration leads to broad smeared features since different pairs show slightly different distances. However, we could expect some periodicity since the nanoparticles themselves are perfectly ordered and corresponding pairs of distances, especially between Fe and Si atoms should reflect the periodicity of the Fe in the nanoparticle. Inspection of the residual in Fig. 3b indeed reveals such a periodicity of about 12 Å which would correspond to twice the distance of Fe-Fe in SNP. An interesting result is that in one nanopore with 6 nm in diameter about 113 unit cells of SNP (6 nm particle) are incorporated and with Z = 4 (cell unit formula) only 392 molecules are needed to form nanoparticles of SNP with clearly visible maxima in the diffracted intensity. This example clearly illustrates that the d-PDF approach is very helpful in the study of host-guest systems, since it limits the following modelling to the guest species and thus simplifies considerably the task. Especially the d-PDF reduces the difficulties owing to overlapping peaks from host and guest as present in the total PDF of the host-guest system. Nevertheless, as for all PDF measurement a high resolution and good statistics are mandatory. This approach was also applied successfully to probe the structural information of a wide variety of host-guest materials, including other coordination framework materials, porous carbons, Prussian Blue analogues and light element nanocomposites[36–38]. Since NMR provides chemical resolution, NMR distinction between the host and the guest ions and counter-ions is trivial due to their different composition (^{29}Si, ^{13}C, ^{23}Na). Therefore the limiting factor remains the relatively low sensitivity inherent to the NMR technique. Nevertheless, even for heterogeneous systems, like the one studied here, we could detect the presence of nanocrystalline particles both from the signal of the nitroprussiate ions (^{13}C) and Sodium counterions (^{23}Na) and this without isotopical labelling.

Concerning the crystallinity and particle size of the embedded species, the PDF analysis provides very detailed insight. As shown above, it relies only on the structural model of the bulk material and a simple envelope function. This type of analysis is very sensitive to the particle size and form[39,40] because the relative strengths of the G(r) amplitudes depend on the number of pairs present at a defined distance r. Additionally, different envelope functions are available in the analysis software to simulate different particle shapes[33,40]. More difficult is the analysis in the case of partial crystallinity or if a large distribution of particle size is present. If the deviation from perfect crystallinity is small, this would be reflected in the width of the G(r) amplitudes. Since this effect is superposed to other contributions, such as thermal motion or other kinds of dynamical behaviour, a deconvolution is necessary which is non-trivial. In all these cases the NMR analysis provides essential and complementary structural information since NMR probes the local structure and rotational dynamics. As demonstrated for our case, the study of counter ions can be

especially suited to answer this question since both elements of the complex show important differences in the NMR signal between the crystalline, amorphous and liquid states. By evaluation of the area of the corresponding NMR lines it is even possible to quantitatively determine the ratio between different distinct physical states of the guest. This is essential in the assessment of such materials with respect to stability and applications, as illustrated on the example of solubility of SNP as a function of the surrounding humidity level. Even if we suggest that the solvated SNP complexes form a contact layer around the nanocrystals inside the pores, the question of the location of the liquid like molecules in the matrix is not fully answered. The fast spin lattice relaxation rates (~1ms) of the ^{23}Na nuclei, as well as the low sensitivity of the ^{13}C nuclei, prevented the use of 2D chemical exchange NMR experiments which could address this point. Future work on ^{13}C, ^{15}N isotopically labelled composites studied at variable temperatures should bring more quantitative insight into the dynamics of the confined complexes.

Conclusions

We have shown on the example of SNP@SiO_2 that the combination of NMR and total X-ray scattering coupled to PDF analysis allows for a detailed structural description of the embedded guest in a porous host. We found that "bulk like" crystalline nanoparticles of SNP can be grown inside porous SiO_2 matrices having a pore diameter as small as 6nm. This result is quite exceptional since the pore diameter is only about ten times larger than the complex size. We also show that the average nanoparticle size is about 6nm which means that they almost completely fill the matrix pores. Nevertheless we found that this crystallinity is still partial since two distinct physical states of SNP are detected. Since crystalline nanoparticles and solvated complexes of SNP could be clearly distinguished, their evolution could thus be investigated as a function of external parameters. We applied this method to study the stability of the SNP host, a prototype of an API, and could show that as a function of atmospheric relative humidity, the ratio between "liquid-like" and nanocrystalline SNP changes. These dissolution properties are not observed for bulk SNP exposed to identical conditions. Therefore this might be useful for the pharmacological application of SNP, since as a function of particle size the solubility-rate can be tailored and it can thus be adapted to the purpose defined bioavailability. In any case, this method can also be used to study crystallization behaviour inside functional materials and to learn more about the thermodynamics in nano-sized systems as well as early stages of crystallization.

Acknowledgements

This work was supported by the Université de Lorraine, the CNRS and the Institut Jean Barriol which are gratefully acknowledged. T. W. is very grateful for his stay as invited professor at the CRM2, Université de Lorraine. The authors from the PhLAM thank the "Fonds Européen de Développement Economique Régional" and the Labex CEMPI and Equipex FLUX through the "Programme Investissements d'Avenir".

Notes and references

[a] Université de Lorraine, CRM2, UMR 7036, Vandoeuvre-les-Nancy, F-54506, France.
[b] CNRS, CRM2, UMR 7036, Vandoeuvre-les-Nancy, F-54506, France.
[c] Institut für Strukturphysik, TU Dresden, Zellescher Weg 16, Dresden, Germany.
[d] Crystallography and Structural Physics, University of Erlangen-Nürnberg, Staudtstr. 3, D-91058 Erlangen, Germany.
[e] Laboratoire de Physique des Lasers, Atomes et Molécules (PhLAM), CNRS (UMR 8523), IRCICA (CNRS, USR 3380), Bâtiment P5, Université Lille 1-Sciences et Technologies, F-59655 Villeneuve d'Ascq Cedex, France.

† Footnotes should appear here. These might include comments relevant to but not central to the matter under discussion, limited experimental and spectral data, and crystallographic data.

Electronic Supplementary Information (ESI) available: [details of any supplementary information available should be included here]. See DOI: 10.1039/b000000x/

1. C. Barbé, J. Bartlett, L. Kong, K. Finnie, H. Q. Lin, M. Larkin, S. Calleja, A. Bush, and G. Calleja, *Adv. Mater.*, 2004, **16**, 1959–1966.
2. J. Li, L. Xu, H. Liu, Y. Wang, Q. Wang, H. Chen, W. Pan, and S. Li, *Int. J. Pharm.*, 2014, **467**, 9–18.
3. C. Argyo, V. Weiss, C. Bräuchle, and T. Bein, *Chem. Mater.*, 2014, **26**, 435–451.
4. H. Yan, C. Teh, S. Sreejith, L. Zhu, A. Kwok, W. Fang, X. Ma, K. T. Nguyen, V. Korzh, and Y. Zhao, *Angew. Chem. Int. Ed.*, 2012, **51**, 8373–8377.
5. D. A. Riccio and M. H. Schoenfisch, *Chem Soc Rev.*, 2012, **41**, 3731–3741.
6. E. Gedat, A. Schreiber, J. Albrecht, T. Emmler, I. Shenderovich, G. H. Findenegg, H.-H. Limbach, and G. Buntkowsky, *J. Phys. Chem. B.*, 2002, **106**, 1977–1984.
7. A. Vyalikh, T. Emmler, I. Shenderovich, Y. Zeng, G. H. Findenegg, and G. Buntkowsky, *Phys. Chem. Chem. Phys.*, 2007, **9**, 2249–2257.
8. T. Azaïs, C. Tourné-Péteilh, F. Aussenac, N. Baccile, C. Coelho, J.-M. Devoisselle, and F. Babonneau, *Chem. Mater.,* 2006, **18**, 6382–6390.
9. G. T. Rengarajan, D. Enke, and M. Beiner, *The Open Physical Chemistry Journal.*, 2007, **1**, 18–24.
10. T. Azais, G. Hartmeyer, S. Quignard, G. Laurent, and F. Babonneau, *J. Phys. Chem. C.*, 2010, **114**, 8884–8891.
11. R. Radhakrishnan, K. E. Gubbins, and M. Sliwinska-Bartkowiak, *J. Chem. Phys.*, 2000, **112**, 11048–11057.
12. C. Alba-Simionesco, B. Coasne, G. Dosseh, G. Dudziak, K. E. Gubbins, R. Radhakrishnan, and M. Sliwinska-Bartkowiak, *J. Phys.: Condens. Matter.*, 2006, **18**, R15.
13. J. Warnock, D. D. Awschalom, and M. W. Shafer, *Phys. Rev. Lett.*, 1986, **57**, 1753–1756.
14. R. Evans and U. M. B. Marconi, *J. Chem. Phys.*, 1987, **86**, 7138–7148.
15. M. Sliwinska-Bartkowiak, G. Dudziak, R. Sikorski, R. Gras, R. Radhakrishnan, and K. E. Gubbins, *J. Chem. Phys.*, 2001, **114**, 950–962.
16. J. Czwartos, M. Sliwinska-Bartkowiak, B. Coasne, and K. E. Gubbins, *pac.*, 2009, **81**, 1953–1959.
17. B. Coasne, J. Czwartos, M. Sliwinska-Bartkowiak, and K. E. Gubbins, *J. Chem. Phys.*, 2010, **133**, 084701.

18. K.-Y. Hsieh, E.-E. Bendeif, A. Gansmuller, S. Pillet, T. Woike, and D. Schaniel, *RSC Adv.*, 2013, **3**, 26132–26141.
19. A. D. Ivankovich, D. J. Miletich, and J. H. Tinker, *Int Anesthesiol Clin.*, 1978, **16**, 1–29.
20. S. K. Wolfe and J. H. Swinehart, *Inorg. Chem.*, 1975, **14**, 1049–1053.
21. M. Goulkov, D. Schaniel, and T. Woike, *J. Opt. Soc. Am. B.*, 2010, **27**, 927–932.
22. D. Schaniel, M. Imlau, T. Weisemoeller, T. Woike, K. W. Krämer, and H.-U. Güdel, *Adv. Mater.*, 2007, **19**, 723–726.
23. E. Berrier, C. Zoller, F. Beclin, S. Turrell, M. Bouazaoui, and B. Capoen, *J Phys Chem B.*, 2005, **109**, 22799–22807.
24. H. El. Hamzaoui, R. Bernard, A. Chahadih, F. Chassagneux, L. Bois, D. Jegouso, L. Hay, B. Capoen, and M. Bouazaoui, *Nanotechnology.*, 2010, **21**, 134002.
25. P. Durand, S. Pillet, E.-E. Bendeif, C. Carteret, M. Bouazaoui, H. El. Hamzaoui, B. Capoen, L. Salmon, S. Hébert, J. Ghanbaja, L. Aranda, and D. Schaniel, *J. Mater. Chem. C.*, 2013, **1**, 1933–1942.
26. S. Brunauer, L. S. Deming, W. E. Deming, and E. Teller, *J. Am. Chem. Soc.*, 1940, **62**, 1723–1732.
27. E. P. Barrett, L. G. Joyner, and P. P. Halenda, *J. Am. Chem. Soc.*, 1951, **73**, 373–380.
28. A. P. Hammersley, S. O. Svensson, M. Hanfland, A. N. Fitch, and D. Hausermann, *High Pressure Research.*, 1996, **14**, 235–248.
29. A. K. Soper and E. R. Barney, *J. Appl. Cryst.*, 2011, **44**, 714–726.
30. A. Khitrin and B. M. Fung, *J. Chem. Phys.*, 2000, **112**, 2392–2398.
31. D. Massiot, F. Fayon, M. Capron, I. King, S. Le Calvé, B. Alonso, J.-O. Durand, B. Bujoli, Z. Gan, and G. Hoatson, *Magnetic Resonance in Chemistry.*, 2002, **40**, 70–76.
32. V. Zorin, *GSim - visualisation and processing tool for NMR experiments and simulations*.
33. R. B. Neder, R. B. & T. Proffen. (2008). *Diffuse Scattering and Defect Structure Simulations: A Cook Book Using the Program DISCUS, IUCr Texts on Crystallography, No. 11*. Oxford University Press.
34. X. Xue and J. F. Stebbins, *Phys Chem Minerals*, 1993, **20**, 297–307.
35. Y. Kim and R. James Kirkpatrick, *Geochimica et Cosmochimica Acta*, 1997, **61**, 5199–5208.
36. K. W. Chapman, P. J. Chupas, and C. J. Kepert, *J. Am. Chem. Soc.*, 2005., **127**, 11232–11233.
37. K. W. Chapman, P. J. Chupas, E. R. Maxey, and J. W. Richardson, *Chem. Commun.*, 2006, 4013–4015.
38. H. Kim, A. Karkamkar, T. Autrey, P. Chupas, and T. Proffen, *J. Am. Chem. Soc.*, 2009, **131**, 13749–13755.
39. C. L. Farrow, C.-Y. Ruan, and S. J. L. Billinge, *Phys. Rev. B.*, 2010, **81**, 134104.
40. K. Page, T. C. Hood, T. Proffen, and R. B. Neder, *J. Appl. Cryst.*, 2011, **44**, 327–336.